

PACS Classification: 79.20.Hx, 82.53.Ps, 61.80. – x

Auger-electron cascades in diamond and amorphous carbon

Beata Ziaja ^{*,†,‡} David van der Spoel ^{*}, Abraham Szöke ^{*,§},
Janos Hajdu ^{* 1}

^{*} *Department of Biochemistry, Biomedical Centre, Box 576, Uppsala University,
S-75123 Uppsala, Sweden*

[†] *Department of Theoretical Physics, Institute of Nuclear Physics, Radzikowskiego
152, 31-342 Cracow, Poland*

[‡] *High Energy Physics, Uppsala University, P.O. Box 535, S-75121 Uppsala, Sweden*

[§] *Lawrence Livermore National Laboratory, Livermore, CA 94551, USA*

Corresponding author:

Janos Hajdu, Department of Biochemistry, Biomedical Centre,
Box 576, Uppsala University, S-75123 Uppsala, Sweden

Tel:+4618 4714999, Fax:+4618 511755, E-mail:hajdu@xray.bmc.uu.se

Manuscript information:

Number of pages:18, Number of figures:9, Number of tables:0

Abstract: We have analyzed the cascade of secondary electrons in diamond and amorphous carbon generated by the thermalisation of a single Auger electron. The elastic electron mean free path was calculated as a function of impact energy in the muffin-tin potential approximation. The inelastic scattering cross section and the energy loss of the electron (expressed in terms of differential inverse mean free path) were estimated from two "optical" models, that utilise the measured dielectric constants of the materials. Using these data, a Monte-Carlo model describing the time evolution of the cascade was constructed. The results show that at most around 20 – 40 secondary

¹e-mail:ziaja@tsl.uu.se, spoel@xray.bmc.uu.se, szoke1@llnl.gov, hajdu@xray.bmc.uu.se

cascade electrons are released by a single Auger electron in a macroscopic sample of diamond or amorphous carbon. Consideration of the real band structure of diamond reduces this number further. The release of the cascade electrons happens within the first 100 femtoseconds after the emission of the primary Auger electron. The results have implications to planned experiments with femtosecond X-ray sources.

1 Introduction

Radiation damage prevents structure determination of single biomolecules and other non-repetitive structures at high resolutions in standard electron or X-ray scattering experiments [1]. Cooling can slow down sample deterioration, but it cannot eliminate damage-induced sample movement within the time needed to complete conventional measurements [1–3]. Emerging new X-ray sources, like free-electron lasers (FEL) [4, 5], will offer new possibilities in imaging. Analysis of the dynamics of damage formation on a sample in an X-ray FEL beam suggests that the conventional damage barrier (about 200 X-ray photons/Å² at 12 keV energy) [2], may be extended substantially at very high dose rates and very short exposure times [6, 7]. A new dynamic barrier of radiation tolerance has been identified at extreme dose rates and ultra short exposure times [4–7]. This barrier is several orders of magnitude higher than previous theoretical limits in conventional experiments. The calculations show that at these extremes, sections of molecular transforms from single macromolecules may be recorded without the need to amplify scattered radiation through Bragg reflections [4, 6].

At 1 Å wavelength, about nine-tenth of the interacting photons will deposit energy into a biological sample, causing damage mainly through the photoelectric effect. The departing photoelectron leaves a hole in a low lying orbital, and an upper shell electron falls into it. This electron may either emit an X-ray photon to produce X-ray fluorescence or may give up its energy to another electron, which is then ejected from the ion as an Auger electron. The probability of fluorescence emission or Auger emission depends on the binding energy of the electron. In biologically relevant light elements, the predominant relaxation process (> 99%) is through Auger emission, and most photoelectric events ultimately remove two electrons from these elements (C, N, O, S). The two electrons have different energies and leave the atom at different times (for a more detailed description, see [6, 8, 9]).

In very small samples (like atoms and single molecules), the primary photoelectrons and the Auger electrons may escape from the sample without further interactions. However, in larger samples, these electrons will become trapped and thermalised. Thermalisation involves inelastic electron-atom interactions, producing secondary cascade electrons. Here we analyze the specific contribution of Auger electrons to the ionization of a macroscopic sample through secondary cascade processes. We selected two different carbon compounds (diamond and amorphous carbon) as models for the calculations.

Auger electrons and photoelectrons propagate through the medium in a different

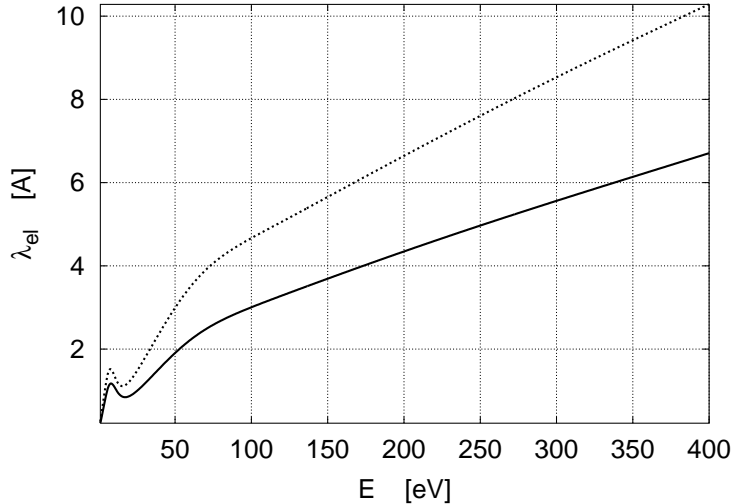


Figure 1: Elastic mean free path (λ_{el} or EMFP) of electrons in diamond or amorphous carbon plotted as a function of electron energy E . Solid line corresponds to the EMFP of electron in diamond, dotted line shows the EMFP of electron in amorphous carbon.

manner. Their de Broglie wavelengths are $\lambda_{Auger} \approx 0.8 \text{ \AA}$ and $\lambda_{photoel} \approx 0.1 \text{ \AA}$, respectively, and λ_{Auger} is comparable with atomic size. This implies that Auger electrons interact multiply with neighbouring atoms, while moving through the system of atoms in the solid [10]. Moreover, since the energy of Auger electrons is low (around 0.25 keV), the interaction potential must include a non-local exchange term which makes accurate description of the interaction complicated. In contrast, photoelectrons propagate almost freely through the medium, and their interaction with (single) atoms in the medium is well described by the Born approximation [11, 12]. Therefore, in samples of intermediate size the low energy Auger electrons are more likely to cause significant ionization than the higher energy photoelectrons. The energy dependence of the mean free path (MFP) of electrons [13, 14] in carbon implies that the MFP of a photoelectron is of the order of hundred Ångstroms whereas the MFP for the Auger electron is only a few Ångstroms ($\geq 4 \text{ \AA}$). This implies that in samples of intermediate size a photoelectron scatters only a few times before leaving the interaction region, while the Auger electron will have multiple interactions.

In section 2 we quantify the elastic and inelastic interactions of Auger electrons with atoms within a solid. Using a Monte-Carlo (MC) simulation we then model the secondary electron cascade caused by inelastic interactions of the primary electron and subsequent secondary electrons with atoms. In section 3, the results of 500 computer simulations of different cascades are presented. These results give the estimated average ionization rate as a function of time. Finally, in section 4 we list our conclusions.

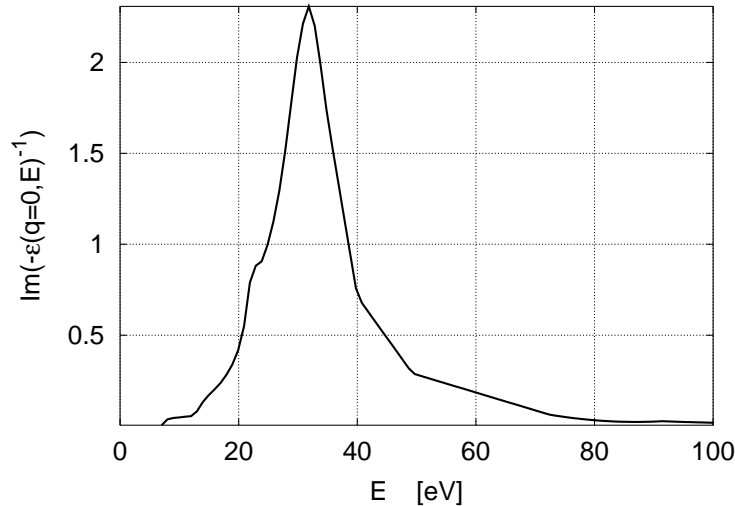


Figure 2: Energy loss function, $Im[-\epsilon(q = 0, E)^{-1}]$ for diamond plotted as a function of photon impact energy E .

2 Secondary electron cascade in a solid

Our study of the secondary electron effects was performed for two forms of carbon: diamond ($\rho = 3.51 \text{ g/cm}^3$) and graphite-like amorphous carbon ($\rho = 2.21 \text{ g/cm}^3$).

Low energy electrons ($E \approx 250 \text{ eV}$) may undergo elastic and inelastic collisions with atoms (electrons and nuclei) in a solid. Since the corresponding electron wavelength is comparable with atomic dimensions, multiple scattering of the electron [15] on neighbouring atoms have to be calculated quantum-mechanically (QM). The QM exchange terms must then be incorporated into the interaction potential.

2.1 Elastic scattering

Calculation of elastic scattering amplitudes and angular distributions can be done accurately by the partial wave expansion technique [11, 12]. In particular, the differential elastic cross-section $\frac{d\sigma_{el}}{d\theta}(E)$ for scattering of an electron on the atom is expressed, using the phase shift δ_l of each partial wave as follows [11, 12] :

$$\frac{d\sigma_{el}}{d\theta}(E) = \frac{2\pi}{k^2} \left| \sum_{l=0}^{\infty} (2l+1) \sin(\delta_l) P_l(\cos(\theta)) \right|^2, \quad (1)$$

where k is the wave number, corresponding to the electron impact energy E , $P_l(\cos(\theta))$ denotes the Legendre polynomial of order l , θ is the scattering angle and the sum goes

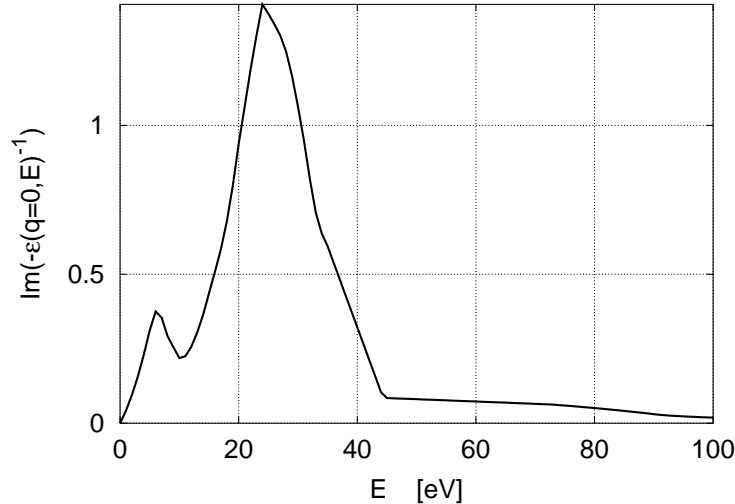


Figure 3: Energy loss function, $Im[-\epsilon(q=0, E)^{-1}]$ for amorphous carbon plotted as a function of photon impact energy E .

over all partial wave contributions $l = 0, \dots, \infty$. The total elastic cross-section $\sigma_{el}(E)$ may be obtained from (1) by integration over θ . The corresponding elastic mean free path, (EMFP) λ_{el} [13, 16] can be calculated as :

$$\lambda_{el}^{-1}(E) = N \sigma_{el}(E), \quad (2)$$

where N denotes the atomic density in the solid. In order to obtain the phase shifts, δ_l in (1), one should solve the respective radial wave equations for each partial wave with the approximate form of the exchange potential. To perform these calculations we used programs from the Barbieri/Van Hove Phase Shift package [17]. First we determined the radial charge density for a free atom, then calculated the radial muffin-tin potential [10, 15] for atoms embedded in a solid (using various approximations to the exchange potential), and finally derived phase shifts from the muffin-tin potential. Multiple elastic scattering within a finite cluster, provided the resulting amplitude was large enough, was included in the calculations. Figure 1 shows the resulting EMFP for diamond and amorphous carbon. For large energies, the EMFPs for both diamond and amorphous carbon increase linearly with electron impact energy. They also scale properly with the medium density, $\frac{\lambda_{el,diamond}(E)}{\lambda_{el,carbon}(E)} \approx \frac{\rho_{carbon}}{\rho_{diamond}}$ (cf. [14, 18]). With decreasing energy the EMFPs decrease monotonically until they show oscillatory features due to interference between low-order scattering waves.

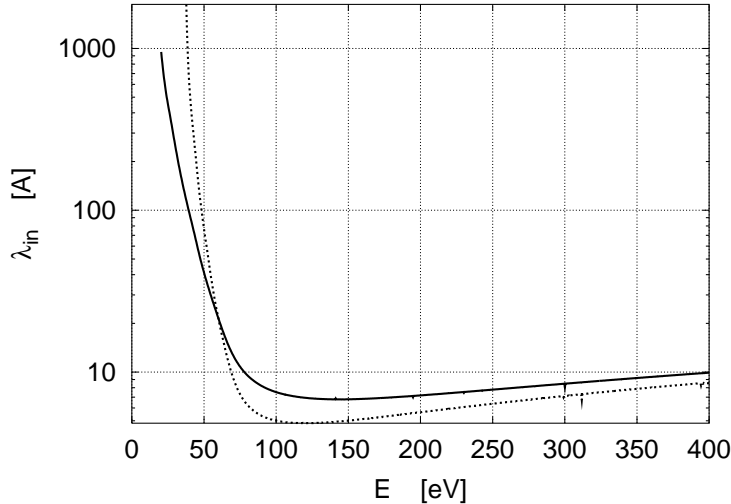


Figure 4: Inelastic mean free path (λ_{in} or IMFP) of electrons in diamond plotted as a function of electron energy E . Solid line corresponds to the IMFP calculated from Ashley's model (9), dotted line shows the IMFP calculated from the TPP-2 model (12).

2.2 Inelastic scattering

An accurate treatment of inelastic atom-electron collisions in a solid is more difficult, especially in the case of low energy Auger electrons when multiple scattering is important. In fact, a fully rigorous method for including inelastic scattering is not available so far. Following Fermi's work [19], the passage of a fast charged particle was treated through the linear perturbation caused by its electric field in the solid. Subsequent developments [20–25] made it possible to extend the dielectric formulation in order to provide a more comprehensive description of quantum-mechanical effects in solids.

Generally speaking, the linear response of a solid is described by a generalized dielectric constant, $\epsilon(\mathbf{q}, \omega)$, that depends both on momentum $\hbar\mathbf{q}$ and frequency ω . In quantum mechanics $\hbar\omega$ corresponds to the energy transfer of the incident charged particle to the solid and $\hbar\mathbf{q}$ to its momentum transfer.

It was shown [23] that the imaginary part of the dielectric constant, $Im[-\epsilon(\mathbf{q}, \omega)^{-1}]$, determines the energy loss of the test charge per unit time, dE/dt , by the formula, $dE/dt \sim \int d\mathbf{q} \int d\omega Im[-\epsilon(\mathbf{q}, \omega)^{-1}]$. Therefore $Im[-\epsilon(\mathbf{q}, \omega)^{-1}]$ is often called the energy loss function (ELF). It satisfies the oscillator-strength sum rule [18], that relates the total energy loss to an effective number of free electrons per atom, Z_{eff} :

$$Z_{eff} = \frac{2}{\pi\hbar^2\Omega_P^2} \int_0^\infty dE E Im[-\epsilon(\mathbf{q}, E/\hbar)^{-1}], \quad (3)$$

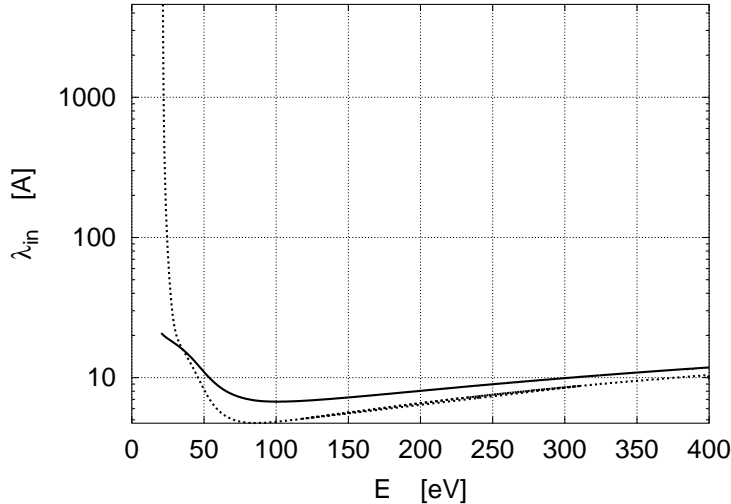


Figure 5: Inelastic mean free path (λ_{in} or IMFP) of electrons in amorphous carbon plotted as a function of electron energy E . Solid line corresponds to the IMFP calculated from Ashley's model (9), dotted line shows the IMFP calculated from the TPP-2 model (12).

where $\Omega_P = \sqrt{(4\pi n_a e^2)/m_e}$, $n_a = N_A \rho/A$ is the density of atoms, N_A is Avogadro's number, ρ is the density of the solid, A is the atomic weight, and E is the energy loss of the incoming test particle.

The energy loss of Auger electrons in a solid is dominated by the excitation of plasmons. At first, we expect this behavior in metals, where conduction electrons form a jellium-like plasma, but not in good insulators. Nevertheless, in all solids the energy loss is dominated by the excitation of valence electrons to the conduction band. The excited electron, in turn, interacts strongly with all other valence electrons. The resultant eigenstate is a plasma resonance. A more familiar result of similar interactions among atoms in a solid is the formation of optical phonons. As expected, the plasmon interacts strongly with the incident Auger electron. For a more quantitative explanation, let us examine the dielectric function $\epsilon(\mathbf{q}, \omega)$. It shows the importance of collective modes for the energy loss of charged particles. If one rewrites, $\epsilon = \epsilon_1 + i\epsilon_2$ then $Im[-\epsilon^{-1}] = \epsilon_2/(\epsilon_1^2 + \epsilon_2^2)$. Since ϵ_2 is small, if ϵ_1 goes to 0 at a certain frequency $\omega = \omega_P$, the ELF, $Im[-\epsilon^{-1}]$, peaks sharply at this frequency. This corresponds to excitation of plasma modes of frequency ω_P by the incoming particle. Therefore, approximating the solid as a gas of free electrons, models the electron energy loss well. As the width of the plasma resonance and its amplitude depend on the details of the plasmon coupling and its decay, accurate results can be expected only from detailed simulations.

In this paper we apply the Lindhard dielectric function approach together with

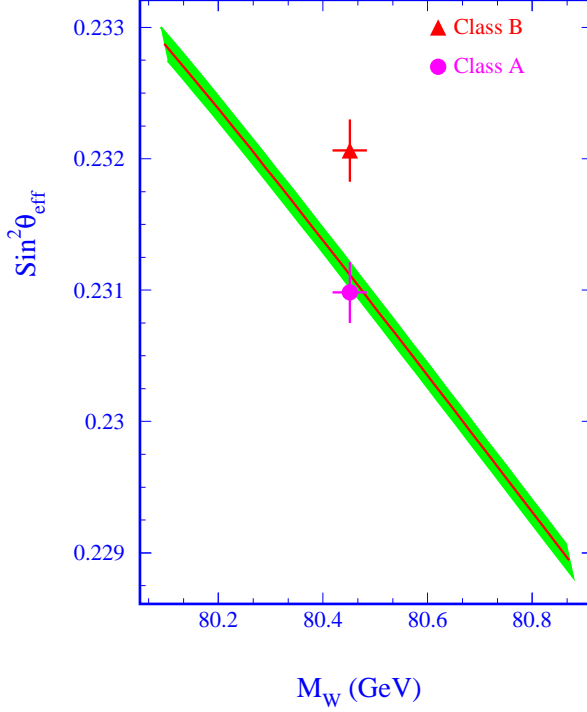


Figure 6: Example of an electron path in a solid.

optical-data models. The approximation proved to work well in free-electron-like materials where the ELF $Im[-\epsilon(0, \omega)^{-1}]$ registered for incoming photons shows a dominant peak due to well-defined volume plasmons [18, 26].

Similarly as above, the response of the medium to a passing electron of a given energy $\hbar\omega$ and momentum $\hbar\mathbf{q}$ is then described by a complex Lindhard dielectric function [21] $\epsilon(\mathbf{q}, \omega)$. In general ϵ may be a tensor but it is assumed here that the medium is homogeneous and isotropic. In this case, ϵ is a scalar function which depends only on the magnitude of $\hbar\mathbf{q}$. The probability of an energy loss $\hbar\omega$ per unit distance travelled by a non-relativistic electron of energy E , i.e. the differential inverse mean free path (DIMFP) $\tau(E, \omega)$ [21, 24, 27, 28], then reads :

$$\tau(E, \omega) = \frac{1}{\pi E a_0} \int_{q_-}^{q_+} \frac{dq}{q} Im[-\epsilon(q, \omega)^{-1}], \quad (4)$$

where a_0 is the Bohr radius, and :

$$q_{\pm} = k \left(1 \pm \sqrt{1 - (\hbar\omega/E)} \right) \quad (5)$$

for k denoting the wave number corresponding to electron impact energy E . The expression for q_{\pm} assumes that the energy and momentum transfer for electron moving in the medium is the same as for a free particle in vacuum, i.e. there is no effective mass assumed. Integration of the DIMFP over the allowed values of ω yields the inelastic mean free path (IMFP) through :

$$\lambda_{in}^{-1}(E) = \int d\omega \tau(E, \omega). \quad (6)$$

It follows from (4) that the only quantity needed to evaluate $\tau(E, \omega)$ and $\lambda_{in}(E)$ is the dielectric response function $\epsilon(q, \omega)$. However, most existing data on dielectric response functions were obtained from photon scattering on solids, for which the momentum transfer is zero. The problem is how to predict the dielectric response function with $q > 0$, knowing only its optical limit ($q = 0$) [27, 28]. For that purpose a phenomenological optical model approach was introduced, where $Im[-\epsilon(q, \omega)^{-1}]$ is expressed via the convolution of $Im[-\epsilon(q = 0, \omega)^{-1}]$ with some profile function of q and ω .

The two transparent optical models we apply hereafter were chosen to give a reasonable estimate of ionization rate within the accuracy required for our model. In what follows we will use atomic units ($\hbar = e = m = 1$) if not stated explicitly.

The optical model by Ashley [27, 28] includes exchange between the incident electron and the electron in the medium modeled in analogy with the structure of the non-relativistic Møller cross-section :

$$\begin{aligned} \tau_A(E, \omega) &= \frac{1}{2\pi E} \int_0^{\infty} d\omega' \omega' Im[-\epsilon(0, \omega)^{-1}] \\ &\times \{F(E, \omega', \omega) + F(E, \omega', E + \omega' - \omega) - \sqrt{F(E, \omega', \omega)F(E, \omega', E + \omega' - \omega)}\}, \end{aligned} \quad (7)$$

where :

$$F(E, \omega', \omega) = \bar{\Theta}(\omega - q_-^2/2 - \omega' > 0) \bar{\Theta}(\omega' + q_+^2/2 - \omega > 0) \frac{1}{\omega(\omega - \omega')}, \quad (8)$$

and $\bar{\Theta}$ is the step function. Substituting (8) into (7) one obtains [27, 28] :

$$\begin{aligned} \tau_A(E, \omega) &= \frac{1}{2\pi E} \int_0^{\infty} d\omega' \omega' Im[-\epsilon(0, \omega)^{-1}] \\ &\times \left(\frac{1}{\omega(\omega - \omega')} + \frac{1}{(E + \omega' - \omega)(E - \omega)} - \frac{1}{\sqrt{\omega(\omega - \omega')(E + \omega' - \omega)(E - \omega)}} \right) \\ &\times (\Theta_1(E, \omega', \omega) + \Theta_2(E, \omega', \omega)), \end{aligned} \quad (9)$$

where Θ_1 and Θ_2 restrict the integration region over ω' and ω :

$$\Theta_1(E, \omega', \omega) = \bar{\Theta}(0 < \omega < E/2) \bar{\Theta}\left(0 < \omega' < 2E(\omega/E - 1 + \sqrt{1 - \omega/E})\right), \quad (10)$$

$$\Theta_2(E, \omega', \omega) = \bar{\Theta}(E/2 < \omega < 3E/4) \bar{\Theta}\left(2\omega - E < \omega' < 2E(\omega/E - 1 + \sqrt{1 - \omega/E})\right). \quad (11)$$

The Tanuma, Powell and Penn model (TPP-2) [18] was adopted for calculating the DIMFP and IMFP of electrons in a solid. We have not used the TPP-2 fit for IMFP calculation but derived the DIMFP, and consequently IMFP, explicitly from statistical approximation described in [18]. The DIMFP $\tau_T(E, \omega)$ yields :

$$\begin{aligned} \tau_T(E, \omega) &= \frac{1}{2\pi E} \int_0^\infty d\omega' \omega' \text{Im}[-\epsilon(0, \omega)^{-1}] \\ &\times \frac{1}{\sqrt{c(\omega')^2 - \omega'^2 + \omega^2} \left(\sqrt{c(\omega')^2 - \omega'^2 + \omega^2} - c(\omega') \right)} \\ &\times \bar{\Theta}(q_-^2/2 < \sqrt{c(\omega')^2 - \omega'^2 + \omega^2} - c(\omega') < q_+^2/2), \end{aligned} \quad (12)$$

where $c(\omega') = k_F(\omega')^2/3$, and $k_F(\omega')$ is the Fermi wave number for the free-electron gas with plasma frequency equal to ω' :

$$k_F(\omega') = \left(\frac{3\pi}{4} \right)^{\frac{1}{3}} \omega'^{\frac{2}{3}}. \quad (13)$$

The corresponding IMFP may be obtained after integrating (12) over ω , according to (6), taking into account the following restrictions :

$$(q_-)^2/2 < \sqrt{c^2 - \omega'^2 + \omega^2} - c < (q_+)^2/2, \quad (14)$$

$$E - E_F < \omega, \quad (15)$$

where E_F denotes the Fermi energy (see below). In particular, restriction (14) implies $\omega' < \omega$. The energy loss functions for diamond and amorphous carbon used in these calculations are plotted in Figs. 2 and 3. In order to obtain the ELF for diamond, we have used optical data for diamond [29], [30] ($E < 35$ eV) and X-ray data for scattering of photons on carbon [31] ($E > 49.3$ eV). The ELF in the intermediate region 35 eV $< E < 49.3$ eV was fitted in order to fulfill the oscillator-strength sum rule (3). The ELF for amorphous carbon was obtained from optical data [32] in the region $E \leq 40$ eV and from X-ray data on atomic carbon [31] ($E > 72.4$ eV). As previously, the ELF in the intermediate region was fitted in order to fulfill the oscillator-strength sum rule (3). Both diamond and amorphous carbon show dominant peaks in their ELF, corresponding to well-defined volume plasmons [26] as expected for free-electron-like materials. This means that the Lindhard dielectric function approximation describes these two solids satisfactorily [18].

Figs. 4 and 5 show the IMFPs of electrons in diamond and amorphous carbon, calculated from (9) and (12). The IMFPs increase monotonically with impact energy, however the scaling with the density of the medium is not preserved explicitly. For low energies ($E \approx 50$ eV), the IMFP shows a characteristic rapid increase, and for the TPP-2 model it becomes undefined if approaching the Fermi energy E_F (cf. (15)).

It should be stressed that the first approximations used here give an upper limit for the total number of secondary electrons liberated by an Auger electron. We expect therefore, that in reality, the number of these cascade electrons will be smaller. The present model treats both allotropes of carbon (diamond, an insulator and amorphous carbon, a conductor) as free-electron-like materials, and we model their band structure in a free-electron gas approximation [10]. The Fermi energy for diamond is $E_F = 28.7$ eV, and for amorphous carbon $E_F = 21.1$ eV as obtained from the free-electron gas approximation. We note that the model will give more accurate results by considering the real band structure of the solid. The Fermi level lies then in the middle of the band gap at $T = 0$ K for semiconductors/insulators.

Based on these initial results, we have constructed a model, which describes the time evolution of the secondary electron cascade in diamond and amorphous carbon (cf. [33], [34]). The algorithm for the MC simulation is available from authors.

The model describes the evolution of the cascade in the approximation of independent non-interacting electrons, neglecting long range Coulomb interactions. The latter assumption holds due to the emission time scales and electron energy ranges relevant for the simulation. We assume that on average only **one** elastic or inelastic electron-atom scattering takes place in a cluster of size $\lambda_{el(in)}$. An electron of energy E (cf. Fig. 6) enters the solid and undergoes collisions with the atoms. Depending on the magnitude of the respective cross-sections, either elastic or inelastic collisions occur as a stochastic process (probability of collision $\approx \frac{\sigma_{el(in)}}{\sigma_{el} + \sigma_{in}}$). In elastic collisions, the primary electron travels through the atomic cluster of size $\lambda_{el}(E)$ and leaves after time $\Delta t = \frac{\lambda_{el}(E)}{\sqrt{2E}}$. For an inelastic collision the situation gets more complicated. First, as previously, the electron travels through the atomic cluster of size $\lambda_{in}(E)$. After time $\Delta t = \frac{\lambda_{in}(E)}{\sqrt{2E}}$ it loses part of its energy ω , and transfers it to an electron of energy E_0 in the Fermi band ($E_0 < E_F$). Energy E_0 of the electron in the band is chosen, according to the Fermi density of levels at $T = 0$ K [10] (with no thermal excitations assumed). If the total energy $E_0 + \omega > E_F$, the secondary electron gets excited, and it is emitted instantaneously when the primary electron leaves the cluster. Otherwise, if $E_0 + \omega < E_F$, the primary electron interacts inelastically with electrons in the Fermi band, losing the part of its energy ω , however, no secondary emission occurs in this case. The process continues until the energies of all excited electrons, including the primary one, fall below the Fermi barrier E_F .

For simplicity we have assumed here that there are no thermal excitations in the Fermi band ($T = 0$ K), and this gives an upper limit of maximal ionization. If $T > 0$, then additional low-occupied energy levels above the Fermi energy become available, so

the effective energy barrier becomes higher, and cascading will liberate fewer electrons from the Fermi band.

3 Numerical results

MC simulations showed that the number of cascade electrons converged after five iterations in both samples. A set of 500 simulations was then performed for each of the two samples in order to obtain a time-dependent estimate of the number of ionizations. In these simulations, the energy of the primary electron was fixed at $E = E_F + 250$ eV. Cascading included 1 + 5 interactions (the primary impact and 5 cascade steps). Figure 7 shows the results.

For diamond the average number of ionization events after the first femtosecond was estimated to be ≈ 6 based on Ashley’s model (9) and ≈ 7 based on the TPP-2 model (12). The number of secondary ionizations increased with time, and it saturated within about 40 fs with a total of 37 electrons released at the maximal ionization of ≈ 37 events (Ashley). Saturation was slower with the TPP-2 model (100 fs), and the total number of cascade electrons (about 18) was about the half of those ejected in Ashley’s model. It should be stressed that in the latter case (TPP-2) the average number of ionizations grew slowly with time. The same scenario held also for the cascades in amorphous carbon. Both Ashley’s and the TPP-2 models predicted 6 – 8 ionizations after the first femtosecond. Calculations based on Ashley’s model give a total number of around 40 cascade electrons. These electrons were released within the first 10 fs, after which no more ionizations occurred. Calculations based on the TPP-2 model level out at 100 fs, and the total number of electrons released in the cascade is only about 23.

The IMFP at $E = 250 + E_F$ eV calculated from (9) (Ashley) was larger than the corresponding IMFP from the TPP-2 model (12) for both diamond and amorphous carbon. However, the most probable energy loss at this energy is less than 60 eV in 80 % of the cases as estimated from the integrated energy loss probability density. This implies that the subsequent cascade is dominated by secondary electrons of energy 60 eV and less, and at this energy, the IMFP calculated in the TPP-2 model is larger than the IMFP in Ashley’s model. Therefore, the number of ionizations estimated in Ashley’s model is larger for both diamond and amorphous carbon.

We have also plotted the maximal average ionization as the function of the electron impact energy (cf. Fig. 8). The total number of ionizations increases linearly with

impact energy in the energy range between $100 + E_F$ eV and $300 + E_F$ eV, as expected.

In constructing the model, we laid emphasis on formulating a reliable description of the Auger electron passage through a solid. Therefore we restricted ourselves to an estimation of the upper limit of ionizations caused by a single Auger electron. This approach allowed us to use first-order approximations to model electron-solid interactions. We performed our calculations in the approximation of non-interacting electrons in the cascade, neglecting long range Coulomb interactions. Since the maximal number of ions in the carbonic medium caused by a single primary Auger electron is small ($\approx 20 - 40$) in comparison with the total number of atoms in the sample ($\approx 10^9$ atoms for $(100 \times 100 \times 100)$ nm³ cube), the approximation of neutral atoms for which the values for the IMFP, EMFP and DIMFP were derived is supposed to work well. This approach is expected to be useful for any secondary electron cascade generated by Auger electrons released in photoelectric events.

Moreover, for microscopic samples one may neglect the ionization rate caused by a photoelectron, and then approximate the total ionization rate caused by a single photoelectric event by the Auger-electron ionization rate. This translates into an ionization rate of $\approx 20 - 40$ secondary electrons emitted within the first 100 femtoseconds after the primary electron emission in diamond and amorphous carbon.

Finally, it should be stressed that we modeled the band structure of diamond and amorphous carbon, using a free-electron-gas approximation. This assumption gives an upper estimation of the ionization rate caused by a single Auger electron. Moreover, the secondary electron emission was considered in case of $T = 0$ K (with no thermal excitations in the Fermi band), and this, again, overestimates the maximal number of ionizations. At $T > 0$ K, the effective energy barrier becomes higher, and cascading will excite fewer electrons from the Fermi band than in the case of $T = 0$ K.

If one considers the real band structure of the solid, then the expected total number of electrons ejected in the cascade decreases further as the Fermi level lies in the middle of the band gap at $T = 0$ K (semiconductors/insulators). The effect of including the real band structure on the ionization dynamics is shown in Fig. 9 for diamond, for which the band structure is well established [35–37].

4 Conclusions

The primary photoelectrons and the Auger electrons may escape from very small samples, however, in larger samples, these electrons may become trapped and thermalised.

This process leads to additional ionization and to the deposition of further energy into the sample. Thermalisation involves inelastic electron-atom interactions, and produces secondary cascade electrons on a longer time scale. In this paper, we analyzed the specific contribution of Auger electrons to the overall ionization of a macroscopic sample. The results describe the evolution of Auger-electron cascades in two model compounds, diamond and amorphous carbon, and show that a maximum of 20 – 40 secondary cascade electrons may be released by a single Auger electron within the first 100 femtoseconds following the emission of the Auger electron. A quantitative description of the ionization dynamics of target samples is of crucial importance to practically all planned experiments at X-ray free-electron lasers, ranging from imaging to the creation of warm dense matter.

Acknowledgments

We are grateful to Gyula Faigel, Zoltan Jurek, Michel A. van Hove, Leszek Motyka, Richard Neutze and Remco Wouts for discussions. This research has been supported in part by the Polish Committee for Scientific Research with grants Nos. 2 P03B 04718, 2 P03B 05119, the EU-BIOTECH Programme and the Swedish Research Councils. A. S. was supported by a STINT distinguished guest professorship. B. Z. was supported by the Wenner-Gren Foundations.

References

- [1] Henderson R. *Q. Rev. Biophys.*, 28:171–193, 1995.
- [2] Henderson R. *Proc. R. Soc. Lond. Biol. Sci.*, 241:6–8, 1990.
- [3] Nave C. *Radiat. Phys. Chem.*, 45:483–490, 1995.
- [4] Hajdu J., Hodgson K., Miao J., van der Spoel D., Neutze R., Robinson C.V., Faigel G., Jacobsen C., Kirz J., Sayre D., Weckert E., Materlik G., and Szoke A. *LCLS: The First Experiments. SSRL, SLAC, Stanford, USA*, 2000.
- [5] Hajdu J. and Weckert E. *TESLA, the Superconducting Electron-Positron Linear Collider with an integrated X-ray Laser Laboratory. Technical Design Report., DESY, ISBN 3-935702-00-0*, 5:150–168, 2001.

- [6] Neutze R., Wouts R., van der Spoel D., Weckert E., and Hajdu J. *Nature*, 406:752–757, 2000.
- [7] Hajdu J. *Curr. Op. Struct. Biol.*, 10:569–573, 2000.
- [8] Dyson N. A. X-rays in atomic and nuclear physics. *Longman, London*, 1973.
- [9] Krause M.O. and Oliver J.H. *J. Phys. Chem. Ref. Data*, 8:329–338, 1979.
- [10] Ashcroft N.W. and Mermin N.D. Solid state physics. *Harcourt, Inc.*, 1976.
- [11] Bransden B.H. and Joachain C.J. Physics of atoms and molecules. *Longman, Essex*, pages 505–513, 1998.
- [12] Burke P.G. Atomic, molecular and optical physics handbook. Editor G.W.F. Drake. *Woodbury, New York American Institute of Physics*, page 536, 1996.
- [13] Powell C. J. *J. Elec. Spec. Rel. Phenom.*, 47:197, 1988.
- [14] Tanuma S., Powell C. J., and Penn D. R. *Surf. Interf. Anal.*, 17:911, 1991.
- [15] Rehr J.J. and Albers R.C. *Phys. Rev. B*, 41:8139–8149, 1990.
- [16] Ashley J.C. *J. Elec. Spec. Rel. Phenom.*, 46:199, 1988.
- [17] Barbieri A. and Van Hove M. A. Private communication. *Phase Shift Package*, <http://electron.lbl.gov/leedpack/>, 2001.
- [18] Tanuma S., Powell C. J., and Penn D. R. *Surf. Interf. Anal.*, 11:577, 1988.
- [19] Fermi E. *Z. Phys.*, 29:315, 1924.
- [20] Pines D. and Bohm D. *Phys. Rev.*, 85:338, 1952.
- [21] Lindhard J. *K. Dan. Vidensk. Selsk. Mat. Fys. Medd.*, 28:1–57, 1954.
- [22] Hubbard J. *Proc. R. Soc. London, Ser. A*, 68:976, 1955.
- [23] Nozières P. and Pines D. *Nuovo Cimento*, 9:470, 1958.
- [24] Ritchie R. H. *Phys. Rev.*, 114:644, 1959.
- [25] Abril I., Garcia-Molina R., Denton C.D., Pérez-Pérez Javier F., and Arista N.R. *Phys. Rev. A*, 58:357, 1998.
- [26] Penn D.R. *Phys. Rev. B*, 13:5248, 1976.

- [27] Ashley J. C. *J. Elec. Spec. Rel. Phenom.*, 50:323, 1990.
- [28] Ashley J. C. *J. Appl. Phys.*, 69:674, 1991.
- [29] Edwards D.F. and Philipp H.R. Handbook of optical constants of solids. Editor E.D. Palik. *Academic Press, New York*, page 666, 1985.
- [30] Philipp H.R. and Taft E.A. *Phys. Rev.*, 136:1445, 1964.
- [31] Henke B.L., Gullikson E.M., and Davis J.C. *Atomic data and nuclear data tables*, 54:211, 1993.
- [32] Cazaux J. and Gramari D. *J. Phys. (France)*, 38:L133, 1977.
- [33] Nishimura K., Kawata J., and Ohya K. *Nucl. Inst. Meth. Phys. Res. B*, 164-165:903, 2000.
- [34] Tanuma S., Ichimura S., and Yoshihara K. *Appl. Surf. Scien.*, 100/101:47, 1996.
- [35] Rohlfing M., Krüger P., and Pollmann J. *Phys. Rev. B*, 48:17791, 1993
- [36] Jiménez I., Terminello L.J., Sutherland D.G.J., and Carlisle J.A. *Phys. Rev. B*, 56:7215, 1997
- [37] Database on Semiconductors <http://www.ioffe.rssi.ru/SVA/NSM/Semicond/>

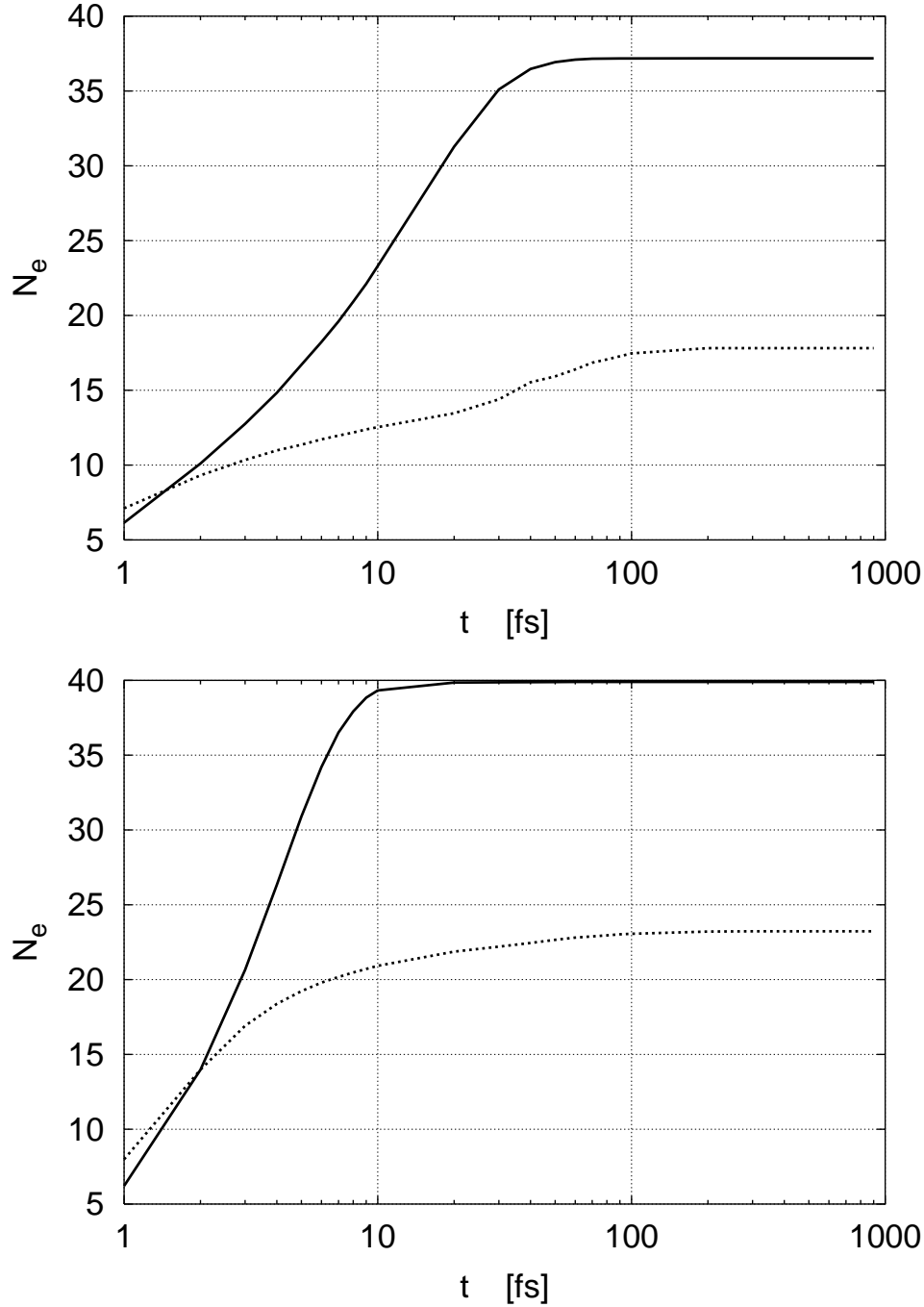


Figure 7: The average ionization rate, N_e , plotted as a function of time, t , for diamond (upper plot) and for amorphous carbon (lower plot). The energy of the primary Auger electron was $E = 250 + E_F$ eV, where E_F is the Fermi energy : $E_F \approx 29$ eV for diamond and $E_F \approx 21$ eV for amorphous carbon. Solid lines correspond to the average ionization estimated from Ashley's model, dotted lines show the average ionization calculated from the TPP-2 model.

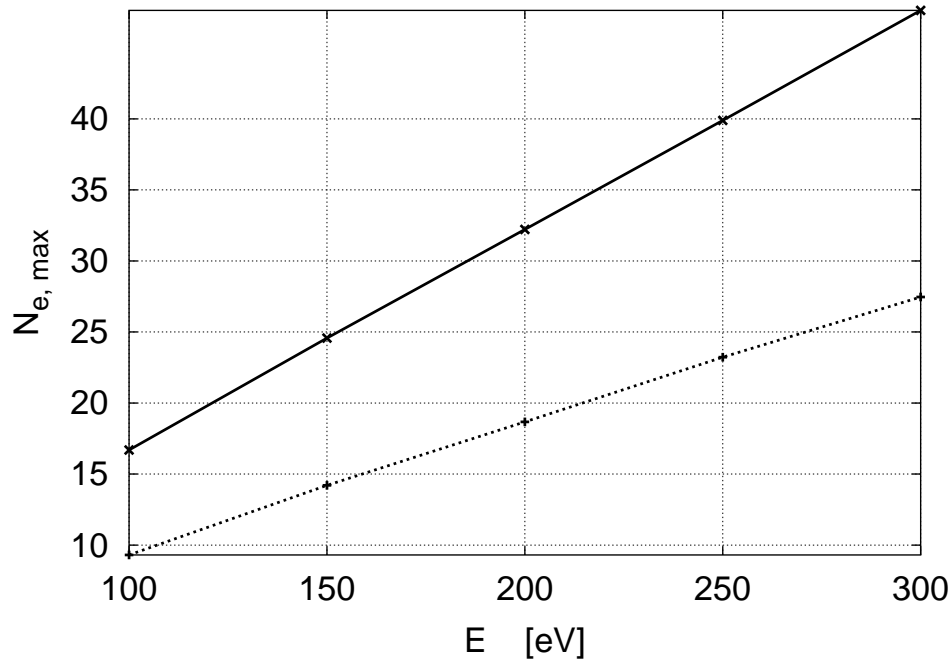
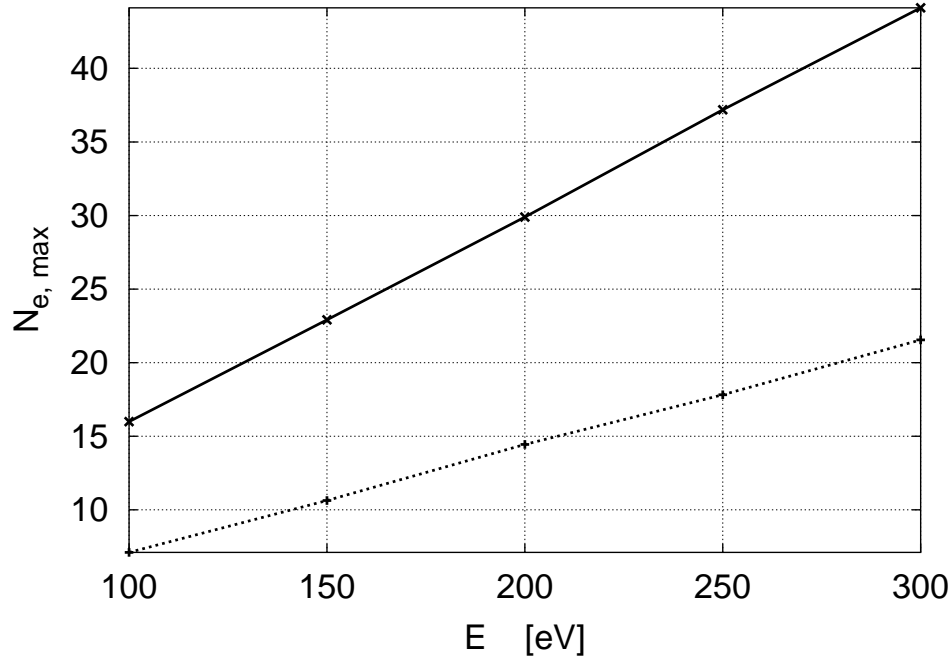


Figure 8: Maximal ionization rate, $N_{e, \max}$, plotted as a function of the energy of the primary Auger electron $E = E' + E_F$ ($E' = 100, 150, 200, 250, 300$ eV) for diamond (upper plot) and for amorphous carbon (lower plot). The corresponding Fermi energies are : $E_F \approx 29$ eV for diamond and $E_F \approx 21$ eV for amorphous carbon. Solid lines show the maximal ionization estimated from Ashley's model, dotted lines show maximal ionization calculated from the TPP-2 model.

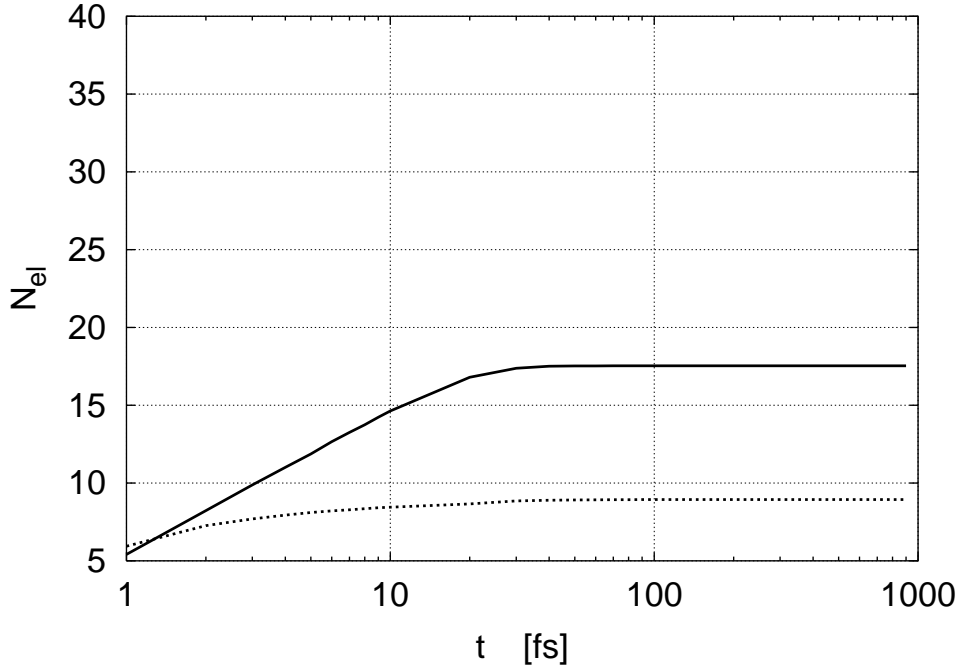


Figure 9: The average ionization rate, N_e , plotted as a function of time, t , for diamond after the real band structure of diamond at $T = 300$ K was included into the model. The energy of the primary Auger electron was $E = 250 + E_F$ eV, where E_F is the Fermi energy : $E_F \approx 29$ eV for diamond. The energy gap at $T = 300$ K equals $E_{gap} = 5.46$ eV. Solid lines correspond to the average ionization estimated from Ashley's model, dotted lines show the average ionization calculated from the TPP-2 model.